Pressure-induced crystal structural and insulator-metal transitions in the quantum spin liquid candidate $CsYbSe_2$

Raimundas Sereika,[1] Xilong Xu,[2] Yizhou Wang,[2] Li Yang,[2] Dongzhou Zhang,[3]
Stella Chariton,[4] Jie Xing,[5] Athena Sefat,[5] Yogesh K. Vohra,[1] and Wenli Bi[1, *]

[1] *Department of Physics, University of Alabama at Birmingham, Birmingham, AL 35294, USA*
[2] *Department of Physics and Institute of Materials Science and Engineering,*
Washington University in St Louis, St. Louis, Missouri 63130, USA
[3] *Hawaii Institute of Geophysics and Planetology,*
School of Ocean and Earth Science and Technology,
University of Hawaii at Manoa, Honolulu, Hawaii 96822, USA
[4] *Center for Advanced Radiation Sources, The University of Chicago, Chicago, Illinois 60637, USA*
[5] *Materials Science and Technology Division, Oak Ridge National Laboratory, Oak Ridge, Tennessee 37831, USA*

$CsYbSe_2$ has an ideal triangular-lattice geometry with pronounced two-dimensionality, pseudospin-1/2 nature, and absence of structural disorder. These excellent characteristics favor a quantum spin-liquid realization in this material. In this work, we applied quasi-hydrostatic compression methods to explore the structural behaviors. Our study reveals that $CsYbSe_2$ undergoes a structural transition around 24 GPa, accompanied by a large volume collapse of $\Delta V/V_0 \sim 13\%$. The ambient hexagonal structure with the space group $P6_3/mmc$ is lowered to the tetragonal structure ($P4/mmm$) under high pressure. Meanwhile, the color of $CsYbSe_2$ changes gradually from red to black before the transition. Dramatic pressure-induced changes are clarified by the electronic structure calculations from the first principles, which indicate that the initial insulating ground state turns metallic in a squeezed lattice. These findings highlight Yb-based dichalcogenide delafossites as an intriguing material to probe novel quantum effects under high pressure.

I. INTRODUCTION

Recently, $YbMgGaO_4$ was proposed as the first rare-earth based, structurally perfect, and two-dimensional triangular antiferromagnet to fulfill a possible experimental realization of the quantum spin-liquid (QSL) with strong spin-orbit coupling (SOC) [1, 2]. Despite the many advantages for potentially hosting QSL state, certain disadvantages were also identified. The anisotropic couplings in the spin space and the bond randomness, caused by the strong spin–orbit entanglements of Yb^{3+} and by the site mixing of Mg^{2+}/Ga^{3+}, respectively, were discerned as two of the most critical obstacles to observe QSL behaviors [3]. Active searches for QSL materials are currently underway and Yb is a favorable key component that plays a critical role. More recently, Yb-based dichalcogenide delafossites formed in the ARX_2 composition (A: alkaline metals, R: rare earth ions, and X: chalcogen) have emerged as QSL and ideal triangular-lattice Heisenberg antiferromagnet candidates which display strong two-dimensionality, effective pseudospin-1/2 nature, and no structural disorder [4–10]. These compounds have a pronounced doublet ground state due to a low-symmetry crystal electric field (CEF) and can be equated or even superior to $YbMgGaO_4$ in terms of the aforementioned characteristics. The strength of Yb delafossites is that they are less prone to defects than the QSL candidate $YbMgGaO_4$.

$CsYbSe_2$, the focus of this work, can be singled out from the ARX_2 group as a significant candidate in the search for QSL behavior and unexplored novel states. The benefit comes from the eight-fold degeneracy of Yb^{3+} ions which could be lifted to four Kramers doublets due to the combined effects of strong SOC and CEF. In fact, the full, theoretically obtained CEF spectrum reveals an intricate and anisotropic energy landscape that is amenable to unconventional magnetism and it is concluded that $CsYbSe_2$ is a strongly XY triangular antiferromagnet [5]. In addition, $CsYbSe_2$ is an insulating $4f$ electronic system. The triangular lattice hosting strongly correlated electrons that are subjected to geometric frustration has been a subject of intense computational and theoretical research [11]. The sister compound $NaYbSe_2$ demonstrates pressure-induced insulator-to-metal transition followed by the emergence of superconductivity [12]. This phase transition has been initially considered as a Mott transition, but later study suggests that $NaYbSe_2$ is a charge-transfer insulator at ambient pressure and reveals a rather complex two-stage process from a band insulator to a semimetal with incoherent Kondo scattering and then to a heavy-fermion metal [13]. Additionally, an intermediate state was predicted to display a delocalization quantum critical point of the Yb1-$4f$ electrons that may explain the observed non-Fermi liquid with linear-in-T resistivity data, while the Yb2-$4f$ electrons should remain localized up to 100 GPa. Comparing $NaYbSe_2$ with $CsYbSe_2$, there are many similarities in terms of chemical composition and physical appearance, but the crystal structures at ambient conditions are different. $NaYbSe_2$ crystallizes in the trigonal crystal system with the space group $R\bar{3}m$ (No. 166) [14], while $CsYbSe_2$ forms in the hexagonal crys-

---

[*] Corresponding author: wbi@uab.edu

tal system with the space group $P6_3/mmc$ (No. 194) [15]. Therefore, $CsYbSe_2$ may behave differently under compression. To investigate $CsYbSe_2$ under high pressure, we combined synchrotron angle-dispersive powder X-ray diffraction (XRD), optical Raman spectroscopy techniques, and first-principles calculations. We have found that $CsYbSe_2$ undergoes a structural transition with a large volume collapse.

II. METHODS

High-quality $CsYbSe_2$ single crystals were grown using the flux method described in detail in Ref. [6]. The obtained samples are considered air-sensitive. Therefore, they were kept in an isolated environment at all times after synthesis. The diamond anvil cell (DAC) technique was used to generate pressure [16]. A general design of the DAC is shown in Fig. 1a. Here, two opposing anvils squeeze the gasket and seal the rim around the chamber, which contains the sample, pressure medium, and Ruby spheres as pressure calibrant. A quasi-hydrostatic high-pressure environment was created by gas or liquid pressure-transmitting medium. The data was then collected through the diamond anvils which serve as an optical window.

The in-situ high-pressure angle-dispersive XRD measurements were carried out at the Beamline 13BM-C (PX^2) of the Advanced Photon Source (APS), Argonne National Laboratory (ANL). The XRD data were collected at room temperature. The wavelength of the x-rays was set to $\lambda = 0.434$ Å and the x-ray beam was focused to 15 μm (v) × 15 μm (h) size. A stainless-steel gasket was prepared to contain the fine powders ground from single crystals of $CsYbSe_2$. Daphne 7575 was used as the pressure-transmitting medium and a ruby sphere was used to determine pressure. The obtained diffraction images were integrated using Dioptas software [17]. Rietveld refinements were performed in GSAS-II software [18].

For the Raman experiments an optical spectroscopy system [19] was exploited at Sector 13 (GeoSoilEnviroCARS, University of Chicago) of the APS, ANL. Measurements were performed in two runs using stainless-steel gaskets to contain the sample, ruby spheres to measure pressure, and a pressure-transmitting medium. In the first run pressure was limited to 16.3 GPa due to technical difficulties and, therefore, did not reach the phase transition pressure. In the second run, Raman data were collected under pressure as high as 28.9 GPa. It is noted that in the first run neon was used as pressure-transmitting medium and in the second run silicone oil was used. In both runs, a laser wavelength of 532 nm was used with a constant power of 20 mW for each spectrum.

Electronic structure calculations were performed using the VASP software package [20, 21], which is based on the linear combination of pseudo-atomic-orbital basis formalism. The exchange-correlation energy was treated within the generalized gradient approximation (GGA) using the Perdew–Burke–Ernzerhof (PBE) functional [22]. For Yb atoms, we used the Yb_3 pseudopotential with Yb-4f orbitals frozen in the core to reduce the computational cost and to get the correct band structures. In turn, band structures were examined following the general path through the Brillouin zone of the given lattices [23]. A 420 eV cut-off was used for the plane-wave basis set and 15 × 15 × 5 k-point sampling is adopted for the unit cell of the $P6_3/mmc$ structure and for the supercell 1 × 1 × 2 of the $P4/mmm$ structure. The Rk_{max} was set to 7 (R is the radius of the smallest muffintin sphere, and k_{max} is the largest k vector in the plane wave expansion). In this case, 432 and 546 k-points in the irreducible part of the Brillouin zone were used for $P6_3/mmc$ and $P4/mmm$ phases, respectively.

III. RESULTS

A. Structural transition under high pressure

The high symmetry of ARX_2 compounds have different packing structures, where rare-earth ions usually form triangular lattices with different alkaline metal-dependent intralayer and interlayer distances. A rather comprehensive study identified that compounds in the $CsRSe_2$ (R = La-Lu) series crystallize in either trigonal ($R3\bar{m}$) or hexagonal ($P6_3/mmc$) crystal systems, depending upon the size of the R^{3+} ion [6]. The difference between these two polymorphs is the stacking of the planar layers in the c direction. It is noted that geometrically frustrated $LiYbSe_2$ adopts a 3D cubic pyrochlore structure with a space group of $Fd3\bar{m}$ which is distinct from the regular delafossites [24]. This indicates that alkaline metal itself in ARX_2 composition can cause a strong impact on the crystal structure. The hexagonal $CsYbSe_2$ in the space group of $P6_3/mmc$ (No. 194) has the lattice parameters $a = b = 4.1539$ Å, and $c = 16.508$ Å [15]. The 2D layers composed of $YbSe_6$ octahedra are stacked along the c-axis with an interlayer distance of 8.25 Å. The Cs cations reside between these layers. A clear 2D nature of $CsYbSe_2$ at ambient pressure is highlighted in Figs. 1b and 1c.

Selected synchrotron powder XRD patterns of $CsYbSe_2$ at different pressures are displayed in Fig. 1d. The low-pressure data match well with the reported ambient hexagonal phase. However, a significant change in the diffraction pattern is observed as pressure is raised above 20 GPa. The appearance of new peaks signals a structural transition, but the sample is still in the mixed phase condition. As pressure is further increased to 27.2 GPa, $CsYbSe_2$ completely transitions to a new phase. The indexing of the high-pressure patterns leads to a tetragonal crystal system which is fully solved to the $P4/mmm$ (No. 123) space group using simulated annealing methods [25–27]. The crystallographic data as well as Rietveld refinement for the high-pressure phase at 36

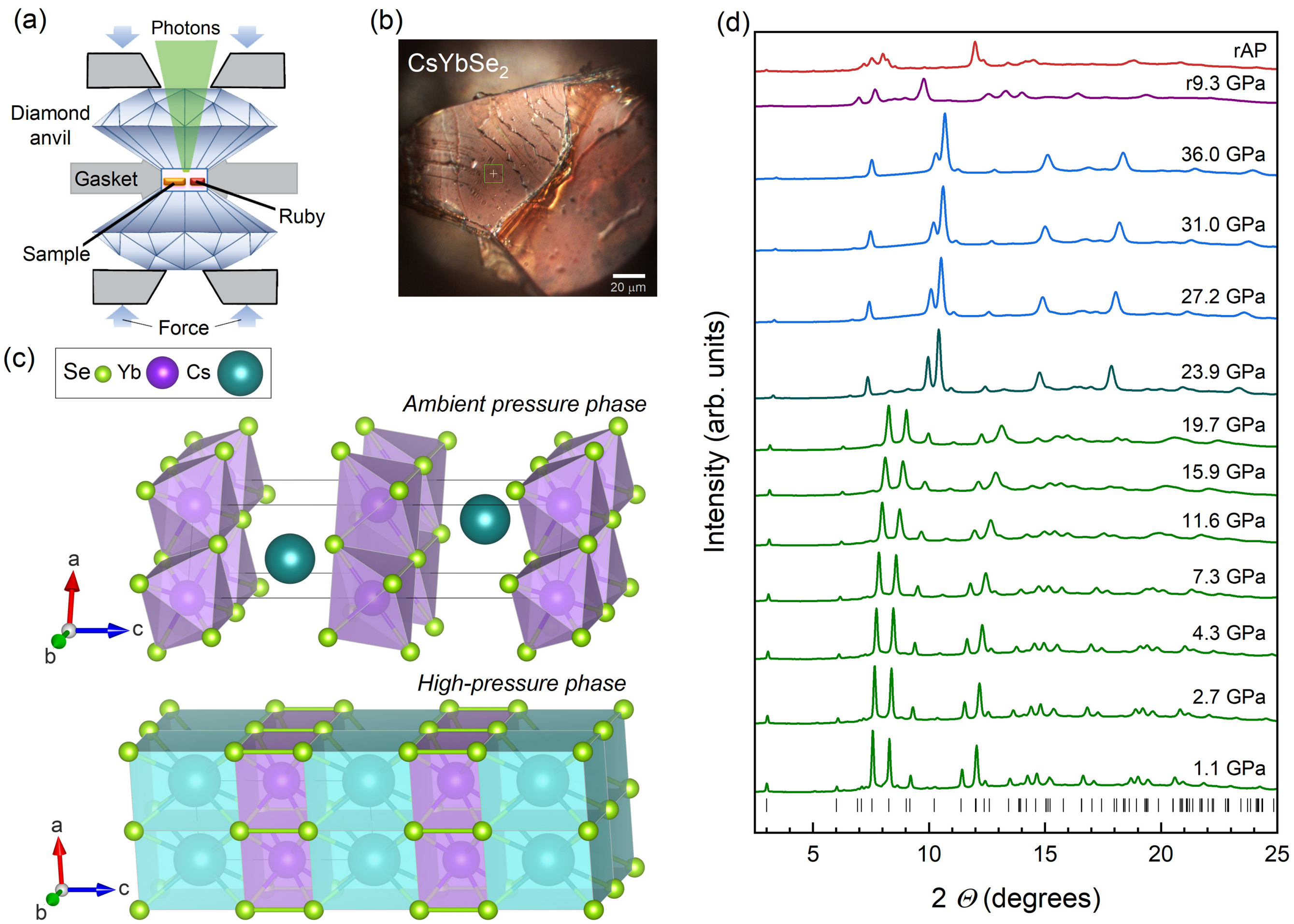

FIG. 1. (a) Schematic of the diamond anvil cell used in the high-pressure experiments. (b) Single crystal of CsYbSe$_2$, highlighting its distinct 2D nature at ambient conditions. (c) Structural view of CsYbSe$_2$ before (space group $P6_3/mmc$) and after (space group $P4/mmm$) the structural transition. (d) Evolution of powder diffraction patterns under various pressures. The data upon decompression is marked with the letter "r". The positions of the initial $P6_3/mmc$ Bragg reflections are marked by vertical bars.

GPa are provided in the Supplemental Material [28] (see Table S1 and Fig. S1).

The high-pressure tetragonal phase is drastically different from the ambient phase. Due to the decreasing lattice volume under high pressure, the reduced distance between 2D layers leads to the formation of new atomic bonds (see Fig. 1c). Consequently, the structure containing YbSe$_6$ and CsSe$_6$ polygons and the polygons observed in this phase become more ordered, with polygonal faces perpendicular to unit cell lattice vectors.

At low pressure CsYbSe$_2$ is a relatively soft material which is typical for materials with layered structures. Under pressure the spacings between the layers shrink more than the chemical bonds between individual atoms. The analysis of the XRD data indicates almost a linear decrease of the lattice parameters as increasing pressure with a minor deviation in the phase transition region (Fig. 2a and b). The high-pressure phase has a higher bulk modulus and higher density than the ambient pressure phase (see Fig. 2d). Across the structural transition a significant collapse in volume is observed with $\Delta V/V_0$ ~ 13%. To estimate the equilibrium bulk modulus, we have fitted the P–V data to the following third-order Birch–Murnaghan equation of state (EoS)[29]:

$$P(V) = \frac{3K_0}{2}\left[\left(\frac{V_0}{V}\right)^{7/3} - \left(\frac{V_0}{V}\right)^{5/3}\right] \left[1 + \frac{3}{4}(K_0' - 4)\left(\left(\frac{V_0}{V}\right)^{2/3} - 1\right)\right], \tag{1}$$

where P, V_0, V, K_0, and K'_0 are pressure, volume at zero pressure, volume under pressure, equilibrium bulk modulus, and its first derivative, respectively. The values of the bulk moduli 45.8 (5) GPa and 79.6 (5) GPa (the first derivative is 4.2) were obtained before and after transition, respectively.

It should be noted that depressurization from 36 GPa to ambient pressure does not result in a full recovery of

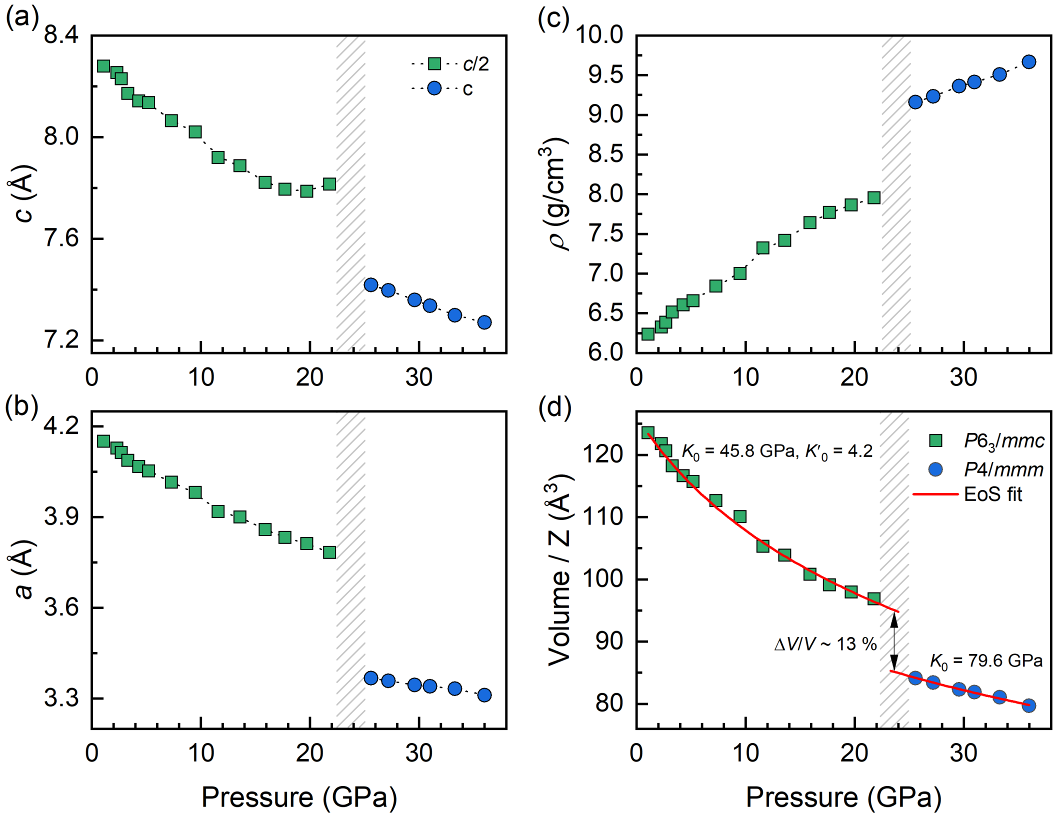

FIG. 2. (a) and (b) Pressure-dependence of the lattice parameters. The dotted lines through the data are guides to the eye. (c) Pressure-dependence of the crystallographic density. (d) Volumes per formula unit as a function of pressure for different phases. The red solid line is the calculated third-order Birch–Murnaghan EoS fit to the experimental data. The bulk moduli (K_0) and the first derivatives (K_0') for the low and high pressure phases are included.

the low-pressure XRD pattern. The irreversible phase transition has also been observed for the $NaYbSe_2$ compound where the high-pressure phase was quenched after pressure was released [12]. However, in $CsYbSe_2$ the XRD pattern after releasing the pressure is distinct from both the initial hexagonal and high-pressure tetragonal phase. Thus, the decompression phenomenon requires more insight and further detailed measurements, which could be addressed in future work. Details on the XRD pattern under decompression are shown in Fig. S2 in the Supplemental Material [28].

B. Optical measurements under high pressure

Symmetry-mode analysis of the atomic displacements predicts 24 normal phonon modes at the Brillouin zone (BZ) center of $CsYbSe_2$[10]: $A_{1g} + 3A_{2u} + 2B_{1u} + 2B_{2g} + E_{1g} + 2E_{2g} + 3E_{1u} + 2E_{2u}$. Here, Raman active modes correspond to non-degenerate A_{1g} symmetry modes, doubly degenerate E_{2g} symmetry modes, and doubly degenerate E_{1g} symmetry modes. The Raman spectra at ambient pressure and low temperatures have been studied previously by performing the Stokes and anti-Stokes measurements and first-principles plane-wave density functional theory calculations. Along with the primary Raman modes, strong CEF excitations have been observed [10]. Primary Raman active phonon modes E^1_{2g}, E^2_{2g}, and A_{1g} were observed experimentally on the Stokes side at 48.0 cm^{-1}, 127.1 cm^{-1} and 169.0 cm^{-1}, respectively. Additional modes originating from CEF excitations appear at low temperature, which are dominated by $4f$ orbitals with degenerated Kramers doublets in the electronic ground state [10].

In our high-pressure experiments, all three Raman active modes (E^1_{2g}, E^2_{2g}, and A_{1g}) observed under ambient conditions can be identified after sample loading in the DAC (see Fig. 3a and Fig. S4 in the Supplemental Material [28]). It should be noted that modes on the anti-Stokes side are naturally weaker than the modes on the Stokes side due to the principle of detailed balance. From the polarization-resolved Raman spectroscopy measurements it is established that the A_{1g} mode is circular only in the parallel (XX) polarization configuration while the E_{2g} is circular under any linear polarization configuration. Interestingly, during compression, a weak A_{1g} mode enhances substantially while the intensity variation of other modes is somewhat smaller (see Fig. 3a and Fig.

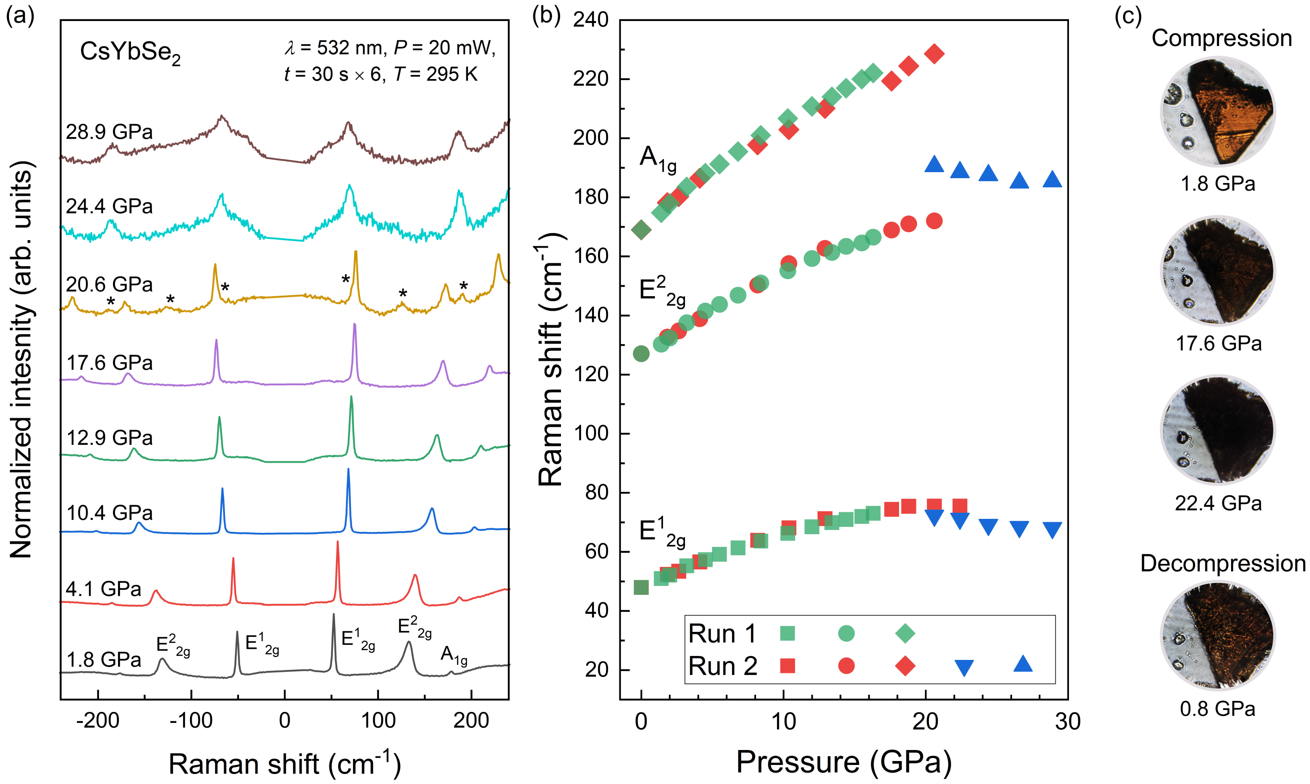

FIG. 3. (a) Selected low energy Stokes and anti-Stokes Raman spectra during CsYbSe$_2$ compression at room temperature in Run 2. Asterisks indicate new peaks which occur during the phase transition. (b) Pressure-dependence of A$_{1g}$, E$^2_{2g}$, and E$^1_{2g}$ Raman modes representing the Stokes side during sample compression. (c) Optical micrographs taken through a microscope during measurements indicate a partially reversible color change.

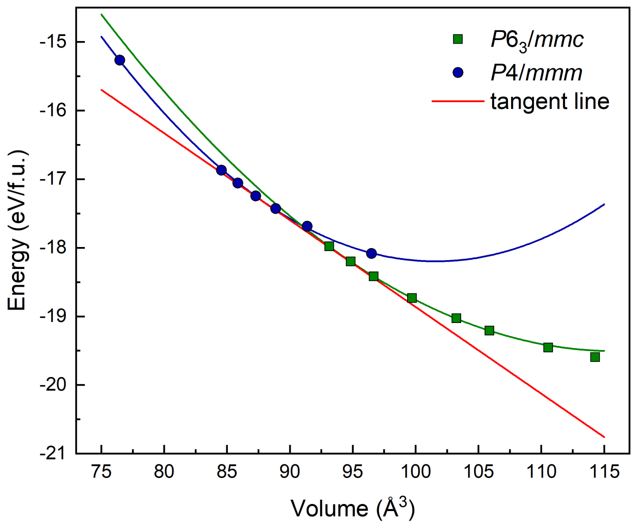

FIG. 4. The energy versus volume for the $P6_3/mmc$ and $P4/mmm$ phases. The red solid line is the common tangent line obtained from the EoS. The green and blue solid lines are fits to the data points representing ambient and high-pressure phases, respectively.

S4). Unfortunately, the CEF excitations are not visible at room temperature, so the behaviors can not be analyzed in this work. To study the behavior of Raman active modes under high pressure, their frequencies were tracked in small pressure steps. As shown in Fig. 3b, all the modes shift to higher energy with increasing pressure up to the critical pressure for structural transition, a typical behavior due to phonon hardening. In the tetragonal phase, the A$_{1g}$ mode which relates to the lattice vibration along the c axis displays steeper pressure dependence than E$^1_{2g}$ and E$^2_{2g}$ modes, likely due to the large reduction of interlayer distance that is shown in the XRD data. A mixed phase is observed at 20.6 GPa, which is in good agreement with the XRD experiment. Three new modes appear at 20.6 GPa with frequencies of 72.3 cm^{-1}, 125.4 cm^{-1}, and 190.6 cm^{-1}. A further increase in pressure completes the transition. The high-pressure phase has drastically reduced the Raman intensity with only two broad modes (see spectra at 24.4 GPa and 28.9 GPa in Fig. 3a). It is noteworthy to point out that the intensity of the new Raman modes decreases gradually with increasing pressure.

Fig. 3(c) shows photographs of CsYbSe$_2$ at various pressures. The sample changes from reddish color to black when it is compressed into the high-pressure phase.

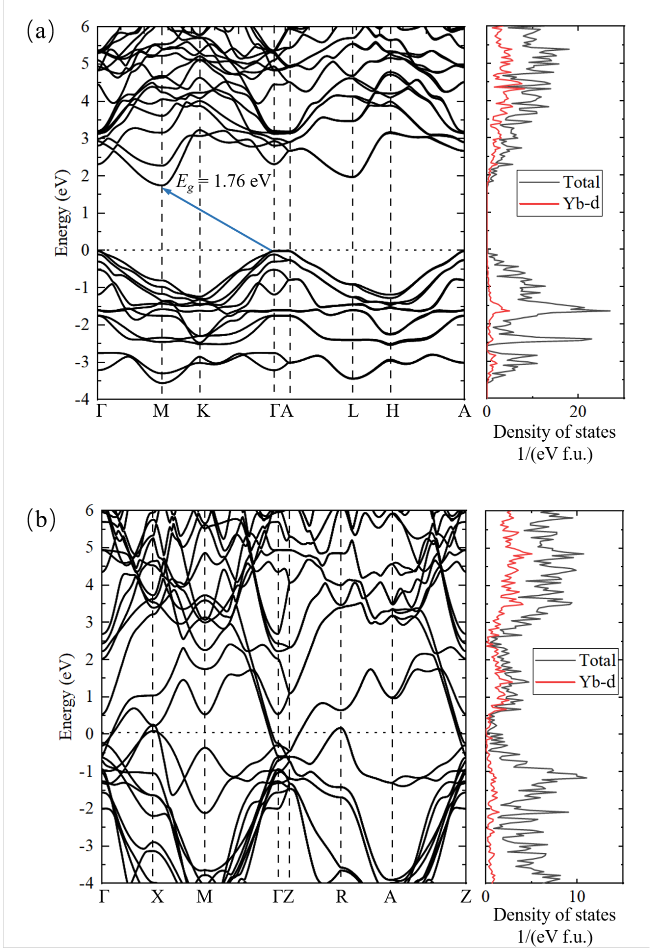

FIG. 5. The band structures and densities of states of $CsYbSe_2$ at (a) ambient pressure and (b) 24 GPa. The black arrow defines the indirect band gap between Γ-M points in the ambient hexagonal $P6_3/mmc$ phase. The figure is plotted using [30].

These color changes coincide with the transition observed in the XRD and Raman measurements. Decompression of the material shows partial color recovery, consistent with the irreversible transition from XRD measurements.

C. First-principles calculations of the structural changes in $CsYbSe_2$

First-principles calculations were carried out to further elucidate effects of the structural phase transition at high pressure. A series of energy calculations with fixed symmetry show that hexagonal ($P6_3/mmc$) structure is energetically favorable at higher volume (lower pressure), whereas tetragonal ($P4/mmm$) is more favored at lower volume (high pressure) (see Fig. 4). The DFT+U method [31] was tested for the d electrons of Yb atoms. U = 2, 4, 6 eV were tested, and it was found that the transition pressure was reduced to 19.0 GPa, 17.7 GPa and 16.3 GPa, respectively. The structural transition from the theoretical calculations is estimated to be at 20.3 GPa (T = 0 K in the DFT simulations) which agrees well with the experimentally observed transition pressure. The calculated band structure at ambient pressure indicates that $CsYbSe_2$ has an insulating band gap of 1.76 eV which is of an indirect type from Γ to M point in the Brillouin zone (Fig. 5a). Our results suggest that the gap value is slightly smaller than that found for $NaYbSe_2$ (the band gap for $NaYbSe_2$ is 1.9 eV) and the other structurally similar rare-earth triangular lattice spin liquid candidates [32]. Furthermore, as shown by the atomic projection density of states in Fig. S5, the top of valence bands is predominantly contributed by the p orbitals of Se atoms, whereas the bottom of conduction bands is primarily contributed by orbitals of Yb atoms, characterizing it as a charge transfer insulator rather than a Mott insulator [33, 34], similar to $NaYbSe_2$ concluded from the band structure calculations [13].

IV. DISCUSSION

The debate on the mechanism of the insulator-to-metal transition and superconductivity in the spin liquid candidate $NaYbSe_2$ under high pressure provides new insights into the potential behavior of delafossites under extreme conditions [13]. Both $NaYbSe_2$ and $CsYbSe_2$ change color gradually with increasing pressure and eventually, appear black. This is directly related to increasing metallicity. However, our observation of $CsYbSe_2$ transitioning to the metallic phase at a much lower pressure of 24 GPa is surprising (insulator-to-metal transition in $NaYbSe_2$ was observed at ~ 60 GPa), considering the fact that the band gap of $CsYbSe_2$ is only slightly smaller than $NaYbSe_2$.

According to our calculations, after the transition to the tetragonal phase, a tremendous expansion of all bands is observed (Fig. 5b). Here, the bandwidth, which is dominantly governed by Yb-d electrons, expands drastically from both conduction and valence bands. The delocalization of the Yb-4f electrons in $CsYbSe_2$ is not obvious since they are frozen. Here, delocalization refers to the spread of electrons across multiple atomic sites, rather than being confined to a single atom. Typically, in rare-earth materials, f electrons are strongly interacting with each other and with the surrounding electrons. As a result, their behavior cannot be properly accounted for within the framework of standard DFT calculations. Therefore, the delocalization process of 4f electrons is debatable and can be further addressed in more detail by using more sophisticated methods, such as dynamical mean-field theory (DMFT).

It is reported that $NaYbSe_2$, a similar QSL candidate system, undergoes an isostructural transition above 12 GPa with the Yb^{3+} triangular lattice maintained in the high-pressure phase [12]. Under further compression to 60 GPa, an insulating to metallic phase transition occurs and subsequently superconductivity emerges above 100 GPa. In the case of $CsYbSe_2$, a hexagonal-to-tetragonal structural transition is observed concurrently with a hexagonal to tetragonal structural transition is observed concurrently with the insulator-to-metal transition, with Yb atoms arranged in the square lattice in the high-pressure phase. Since the QSL state requires the combined effects of spin frustration and crystal electric field, the fate of the ground state in $CsYbSe_2$ requires future experimental and theoretical investigation.

V. CONCLUSIONS

In summary, we have investigated the structural and optical properties of the quantum spin liquid candidate $CsYbSe_2$ under quasi-hydrostatic pressures up to 36 GPa. The synchrotron XRD data reveal a crystal structural transformation around 24 GPa with a large volume collapse of $\Delta V/V_0 \sim 13\%$. The pressure-induced structural transition can be classified as a first-order type. The optical measurements are in good agreement with the structural changes observed with XRD, confirming transition at similar pressure, showing a drastic change of the Raman modes, and revealing a gradual color change with increasing pressure. Using theoretical simulations, we resolve that the structural transition is from the ambient hexagonal $P6_3/mmc$ to the tetragonal $P4/mmm$ phase. The band structure calculations indicate that $CsYbSe_2$ is a charge transfer insulator, similar to $NaYbSe_2$. The observed volume collapse takes place along with the insulator-to-metal transition. In contrast to $NaYbSe_2$, which does not exhibit volume collapse, the metallization process in $CsYbSe_2$ occurs at a much lower pressure. These interesting results warrant further experimental and theoretical studies to elucidate the nature of this transition and explore new quantum phases induced by pressure.

ACKNOWLEDGMENTS

This work was supported by the National Science Foundation (NSF) CAREER Award No. DMR-2045760. L.Y. is supported by NSF Grant No. DMR-2124934. This work uses the Extreme Science and Engineering Discovery Environment (XSEDE), which is supported by NSF grant No. ACI-1548562. The authors acknowledge the Texas Advanced Computing Center (TACC) at The University of Texas at Austin for providing HPC resources. Research at Oak Ridge National Laboratory (ORNL) is supported by the U.S. Department of Energy (DOE), Office of Science, Basic Energy Sciences (BES), Materials Sciences and Engineering Division. This research used resources of the Advanced Photon Source, a U.S. DOE Office of Science user facility operated for the DOE Office of Science by Argonne National Laboratory under Contract No. DE-AC02-06CH11357. Uses of the COMPRES-GSECARS gas loading system and the PX^2 program were supported by COMPRES (NSF grant EAR-1661511) and GSECARS (NSF grant EAR-1634415 and DOE grant DE-FG02-94ER14466). Use of the GSECARS Raman Lab System was supported by the NSF MRI Proposal (EAR-1531583). We thank Dr. Young Jay Ryu for his kind help with gas loading in DACs at the APS.

---

[1] Y. Li, G. Chen, W. Tong, L. Pi, J. Liu, Z. Yang, X. Wang, and Q. Zhang, Phys. Rev. Lett. **115**, 167203 (2015).

[2] Y. Li, H. Liao, Z. Zhang, S. Li, F. Jin, L. Ling, L. Zhang, Y. Zou, L. Pi, Z. Yang, J. Wang, Z. Wu, and Q. Zhang, Sci. Rep. **5**, 16419 (2015).

[3] Y. Li, Adv. Quantum Technol. **2**, 1900089 (2019).

[4] B. Schmidt, J. Sichelschmidt, K. M. Ranjith, T. Doert, and M. Baenitz, Phys. Rev. B **103**, 214445 (2021).

[5] C. A. Pocs, P. E. Siegfried, J. Xing, A. S. Sefat, M. Hermele, B. Normand, and M. Lee, Phys. Rev. Research **3**, 043202 (2021).

[6] J. Xing, L. D. Sanjeewa, J. Kim, G. R. Stewart, M.-H. Du, F. A. Reboredo, R. Custelcean, and A. S. Sefat, ACS Materials Lett. **2**, 71 (2020).

[7] J. Xing, L. D. Sanjeewa, A. F. May, and A. S. Sefat, APL Mater. **9**, 111104 (2021).

[8] P. Bhattacharyya and L. Hozoi, Phys. Rev. B **105**, 235117 (2022).

[9] T. Xie, A. A. Eberharter, J. Xing, S. Nishimoto, M. Brando, P. Khanenko, J. Sichelschmidt, A. A. Turrini, D. G. Mazzone, P. G. Naumov, L. D. Sanjeewa, N. Harrison, A. S. Sefat, B. Normand, A. M. Lauchli, A. Podlesnyak, and S. E. Nikitin, arXiv:2210.04928v2 (2022).

[10] Y.-Y. Pai, C. E. Marvinney, L. Liang, J. Xing, A. Scheie, A. A. Puretzky, G. B. Halasz, X. Li, R. Juneja, A. S. Sefat, D. Parker, L. Lindsay, and B. J. Lawrie, J. Mater. Chem. C **10**, 4148 (2022).

[11] A. Wietek, R. Rossi, F. Šimkovic, M. Klett, P. Hansmann, M. Ferrero, E. M. Stoudenmire, T. Schäfer, and A. Georges, Phys. Rev. X **11**, 041013 (2021).

[12] Y.-T. Jia, C.-S. Gong, Y.-X. Liu, J.-F. Zhao, C. Dong, G.-Y. Dai, X.-D. Li, H.-C. Lei, R.-Z. Yu, G.-M. Zhang, and C.-Q. Jin, Chin. Phys. Lett. **37**, 097404 (2020).

[13] Y. Xu, Y. Sheng, and Y.-F. Yang, npj Quantum Mater. **7**, 21 (2022).

[14] A. K. Gray, B. R. Martin, and P. K. Dorhout, Z. Kristallogr. NCS **218**, 19 (2003).

[15] B. Deng and J. A. Ibers, Acta Cryst. **E61**, i15 (2005).

[16] H.-K. Mao, X.-J. Chen, Y. Ding, B. Li, and L. Wang, Rev. Mod. Phys. **90**, 015007 (2018).

[17] C. Prescher and V. B. Prakapenka, High Press. Res. **35**, 223 (2015).

[18] B. H. Toby and R. B. Von Dreele, J. Appl. Crystallogr. **46**, 544 (2013).

[19] N. Holtgrewe, E. Greenberg, C. Prescher, V. B. Prakapenka, and A. F. Goncharov, High Press. Res. **39**, 457 (2019).

[20] G. Kresse and J. Furthmüller, Comput. Mater. Sci. **6**, 15 (1996).

[21] G. Kresse and J. Furthmüller, Phys. Rev. B **54**, 11169 (1996).

[22] J. P. Perdew, K. Burke, and M. Ernzerhof, Phys. Rev. Lett. **77**, 3865 (1996).

[23] W. Setyawan and S. Curtarolo, Comp. Mater. Sci. **49**, 299 (2010).

[24] R. S. Dissanayaka Mudiyanselage, H. Wang, O. Vilella, M. Mourigal, G. Kotliar, and W. Xie, J. Am. Chem. Soc. **144**, 11933 (2022).

[25] A. Khachaturyan, S. Semenovsovskaya, and B. Vainshtein, Acta Cryst. **A37**, 742 (1981).

[26] W. I. F. David, K. Shankland, and N. Shankland, Chem. Commun. **8**, 931 (1998).

[27] C. I. Choua and T. K. Lee, Acta Cryst. **A58**, 42 (2002).

[28] See Supplemental Material at [link] for additional crystallographic parameters and some additional details on gained results.

[29] F. Birch, Phys. Rev. **71**, 809 (1947).

[30] H. Q. Pham, Mcu: Modeling and crystallographic utilities, 2023, `https://github.com/hungpham2017/mcu`, accessed: Feb 14, 2023.

[31] S. L. Dudarev, G. A. Botton, S. Y. Savrasov, C. J. Humphreys, and A. P. Sutton, Phys. Rev. B **57**, 1505 (1998).

[32] W. Liu, Z. Zhang, J. Ji, Y. Liu, J. Li, X. Wang, H. Lei, G. Chen, and Q. Zhang, Chin. Phys. Lett. **35**, 117501 (2018).

[33] J. Zaanen, G. A. Sawatzky, and J. W. Allen, Phys. Rev. Lett. **55**, 418 (1985).

[34] M. Imada, A. Fujimori, and Y. Tokura, Reviews of Modern Physics **70**, 1039 (1998).